Computational Materials Science 262 (2026) 114399

Contents lists available at ScienceDirect

Computational Materials Science

journal homepage: www.elsevier.com/locate/commatsci

Full length article

Ultrafast quenching leads to nanograined gallium nitride containing superlattice-like multi-phase domains

Mehrab Lotfpour, Haoran Cui, Nolan Hagen, Milad Nasiri, Theodore Maranets, Yan Wang *, Lei Cao *

Department of Mechanical Engineering, University of Nevada, Reno, Reno, 89557, NV, USA

ARTICLE INFO

Keywords:
Gallium nitride
Superlattice
Phase boundary
Thermal conductivity
Ultrafast quenching

ABSTRACT

The microstructural evolution and thermal transport properties of gallium nitride (GaN) subjected to ultrafast melt-quenching are investigated using molecular dynamics simulations. Varying cooling rates lead to distinct nucleation pathways and the formation of defect-rich microstructures comprising zincblende and wurtzite phases, including unique superlattice-like arrangements. Characteristic nucleation cores and a range of defects, including twins, stacking faults, and dislocations, emerge and significantly influence phonon transport. Quenched GaN exhibits ultralow thermal conductivity, with reductions up to 99% compared to pristine GaN, primarily due to phonon scattering at grain and phase boundaries. Notably, coherent zincblende/wurtzite interfaces maintain high thermal conductance owing to efficient phonon mode matching. These findings offer atomistic insights for engineering heat conduction in GaN through controlled microstructural design.

1. Introduction

Gallium nitride (GaN), with its wide direct bandgap of ~3.4 eV, high electron mobility, and exceptional thermal and chemical stability, has emerged as a cornerstone material for high-power-density, high-frequency, and high-temperature electronics and optoelectronics [1,2]. These attributes enable GaN-based devices to function reliably under extreme operating conditions that typically exceed the capabilities of conventional silicon-based technologies.

The performance and versatility of GaN devices depend critically on controlling and engineering its microstructure. Various strategies have been employed toward this goal, including chemical doping [3], strain engineering [4], and the fabrication of nanostructures such as thin films, nanowires, quantum dots, and heterostructure superlattices. Among these approaches, the design of phase-engineered GaN nanostructures offers unique opportunities for tailoring electronic and thermal properties at the atomic scale.

At ambient pressure, GaN crystallizes predominantly in two closely related tetrahedrally coordinated structures: the thermodynamically stable wurtzite (WZ) phase and the metastable zincblende (ZB) phase. The WZ lattice can be derived from the ZB lattice by a relative sliding of successive (111) planes along the [111] direction. Their cohesive energies differ by less than 5 meV/atom (−4.529 eV/atom for WZ and −4.524 eV/atom for ZB), underscoring their near-degeneracy. This small energy difference, combined with their close crystallographic relationship, results in highly coherent ZB/WZ interfaces with low interfacial energy. Importantly, these dual-phase interfaces are chemically homogeneous — comprising only Ga and N atoms — thereby avoiding the detrimental intermixing and defect formation common to heterostructures of different chemistries.

Despite these similarities, the two polymorphs differ in stacking sequence, lattice symmetry, and corresponding physical properties. By combining WZ and ZB domains into a superlattice — hereafter referred to as a ZB/WZ superlattice — one can exploit their distinct electronic structures to realize tunable bandgaps, tailored carrier transport, and potentially enhanced thermal management. This concept mirrors polymorph-engineered heterostructures in other III–V semiconductors, where control over superlattice periodicity enables the realization of tailored optoelectronic properties.

Several studies have reported the synthesis of ZB/WZ superlattices in various semiconductors. For example, Zhang et al. [5] fabricated a $Cd_{1-x}Zn_xS$ semiconductor with a ZB/WZ superlattice structure via an oriented-attachment growth mechanism during nanocrystal coarsening, demonstrating its potential for photocatalytic water splitting. Algra et al. [6] achieved microstructural control in indium phosphide (InP) through zinc doping, enabling the formation of a ZB/WZ twinning superlattice instead of the pure WZ phase. Similarly, Caroff et al. [7] tuned the indium arsenide (InAs) microstructure by varying growth temperature, yielding well-defined ZB/WZ superlattices.

* Corresponding authors.
E-mail addresses: yanwang@unr.edu (Y. Wang), leicao@unr.edu (L. Cao).

https://doi.org/10.1016/j.commatsci.2025.114399
Received 19 September 2025; Received in revised form 1 November 2025; Accepted 17 November 2025
Available online 23 November 2025

Jacobs et al. [8] identified coherent {0001}/{111} ZB/WZ interfaces in GaN nanowires, while Dick et al. [9] produced ZB/WZ twinned superlattices in InAs via metal–organic vapor phase epitaxy (MOVPE), controlling the stacking sequence through adjustments in temperature and V:III precursor ratio. Their work revealed a diversity of nanowire morphologies, including periodically twinned ZB nanowires, ZB/WZ polytypic superlattices, isolated stacking faults, and short WZ segments embedded in ZB. Spirkoska et al. [10] investigated GaAs growth under varying rates and arsenic fluxes, finding conditions that yield either pure ZB or twinned ZB/WZ superlattice structures. In molecular dynamics simulations, Tan et al. [11] observed extensive ZB/WZ twins in melt-quenched GaN. Analogous stacking-disordered structures have also been reported in CdSe and other III–V compounds [12–14], where subtle thermodynamic and kinetic effects mediate the coexistence of hexagonal and cubic polymorphs. Collectively, these studies indicate that small free-energy differences combined with high interfacial coherence favor the co-formation of ZB and WZ domains, particularly under far-from-equilibrium solidification conditions.

Beyond GaN, the controlled coexistence of multiple polymorphs has been widely studied in metals, ceramics, and high-entropy alloys, where cooling rates strongly influence atomic mobility and crystallization pathways [15–20]. Cross-nucleation, where one polymorph nucleates epitaxially on another due to structural compatibility, has been identified as a key mechanism in such systems. For GaN, understanding these polymorphic interactions is not only scientifically intriguing but also technologically significant, as ZB/WZ superlattices could simultaneously reduce defect densities, enable precise bandgap engineering, and improve thermal transport.

Despite these promising prospects, the microstructural evolution of GaN under ultrafast melt-quenching remains largely unexplored. In particular, the atomic-scale mechanisms driving the formation of ZB/WZ twins, coherent interfaces, and superlattice-like domains during rapid solidification are not well understood. This knowledge gap is especially critical given emerging interest in integrating GaN-based heat spreaders or thermoelectric coolers directly into GaN power modules. Such monolithic architectures minimize Kapitza resistance at interfaces, enabling superior heat dissipation and improved device reliability.

Motivated by these challenges, the present work employs large-scale molecular dynamics simulations to investigate the nucleation, growth, and structural organization of GaN during ultrafast melt-quenching. We focus on the emergence of WZ and ZB domains, the formation of twin and grain boundaries, and the development of coherent ZB/WZ superlattice domains. Furthermore, we systematically evaluate the thermal conductivity of the resulting microstructures, with particular emphasis on the role of polymorphic interfaces, grain boundaries, and defect populations.

The remainder of this paper is organized as follows. Section 2 describes the simulation methodology and computational protocols. Section 3 presents the results on microstructural evolution and thermal transport in melt-quenched GaN, followed by discussion of the underlying mechanisms. Finally, Section 4 summarizes our key findings and outlines future research directions.

2. Methodology

2.1. General setup of molecular dynamics simulations

All the molecular dynamics simulations in this study are performed using the LAMMPS Molecular Dynamics Simulator [21]. The atomic interactions within GaN are modeled using the Stillinger–Weber potential [22]. A time integration step of 1 fs is used, and periodic boundary conditions are applied along all three spatial dimensions.

2.2. Melt-quench simulations

Melt-quench simulations are carried out on a WZ GaN structure containing approximately 0.25 million Ga and 0.25 million N atoms, with dimensions of $20.7 \times 17.6 \times 16.6$ nm^3. Initial atomic velocities are assigned randomly according to a Gaussian distribution corresponding to a temperature of 300 K. The system is then heated to 4600 K while maintaining the pressure at 0 Pa, using the isothermal–isobaric (NPT) ensemble with a Nosé–Hoover thermostat and barostat [23,24], as implemented in LAMMPS through the "fix npt" command. The target temperature of 4600 K, significantly exceeding the melting point of GaN, ensures complete melting and atomic diffusion. After reaching 4600 K, the system is equilibrated for 300 ps under the same ensemble conditions. Subsequently, the molten GaN is quenched from 4600 K to 10 K at different cooling rates (0.1, 0.5, and 1 K/ps), while maintaining 0 Pa pressure. Atomic configurations are recorded at intervals of 100 ps, 20 ps, and 10 ps for cooling rates of 0.1, 0.5, and 1 K/ps, respectively, to enable detailed analysis of microstructure evolution during the quenching process.

2.3. Thermal transport modeling

Equilibrium molecular dynamics (EMD) simulations are employed to compute the lattice thermal conductivity (κ) of the GaN structures using the Green–Kubo formalism. Initially, atomic velocities are randomized based on a Gaussian distribution corresponding to an average temperature of 20 K. The system is then gradually heated from 20 K to the target temperature over 0.3 ns using a Nosé–Hoover thermostat and barostat [23,24], followed by a 1.2 ns equilibration. After equilibration, a microcanonical (NVE) ensemble is used for 8 ns to collect the heat flux data necessary for κ calculations.

The lattice thermal conductivity is calculated using the Green–Kubo relation [25]:

$$\kappa = \frac{V}{k_B T^2} \int_0^\infty \langle J(t)J(0)\rangle \, dt, \tag{1}$$

where k_B is the Boltzmann constant, T is the system temperature, V is the simulation cell volume, t is time, and $J(t)$ is the heat flux. $\langle J(t)J(0)\rangle$ represents the heat flux autocorrelation function. Due to the notable noise associated with the Green–Kubo approach, following previous studies [26–28], we perform five sets of independent EMD simulations, which have different initial velocities, for pristine GaN cases, and three sets of independent EMD simulations for melt-quenched GaN and nanograined GaN to minimize the uncertainty in predicting thermal conductivity values. Additional details regarding the Green–Kubo calculations can be found in our previous work [29,30].

While EMD simulations enable evaluation of the bulk thermal conductivity, nonequilibrium molecular dynamics (NEMD) simulations are conducted to study interfacial thermal transport, particularly to determine the interfacial thermal resistance (Kapitza resistance). The leftmost and rightmost atomic layers are fixed to act as boundaries preventing heat leakage. A hot thermostat is applied to the left side to maintain a high temperature, and a cold thermostat to the right side to maintain a low temperature, thereby establishing a steady-state temperature gradient and heat current across the system. More details of the setup of NEMD simulations can be found in our previous study [31].

The interfacial thermal resistance R is calculated as:

$$R = \frac{A_c \cdot \Delta T}{q}, \tag{2}$$

where q is the steady-state heat current, A_c is the cross-sectional area perpendicular to the heat flow, and ΔT is the temperature drop across the interface.

We note at the outset that the Stillinger–Weber interatomic potential used in this study is not parametrized to yield quantitatively accurate values of κ. Instead, our objective is to capture the qualitative

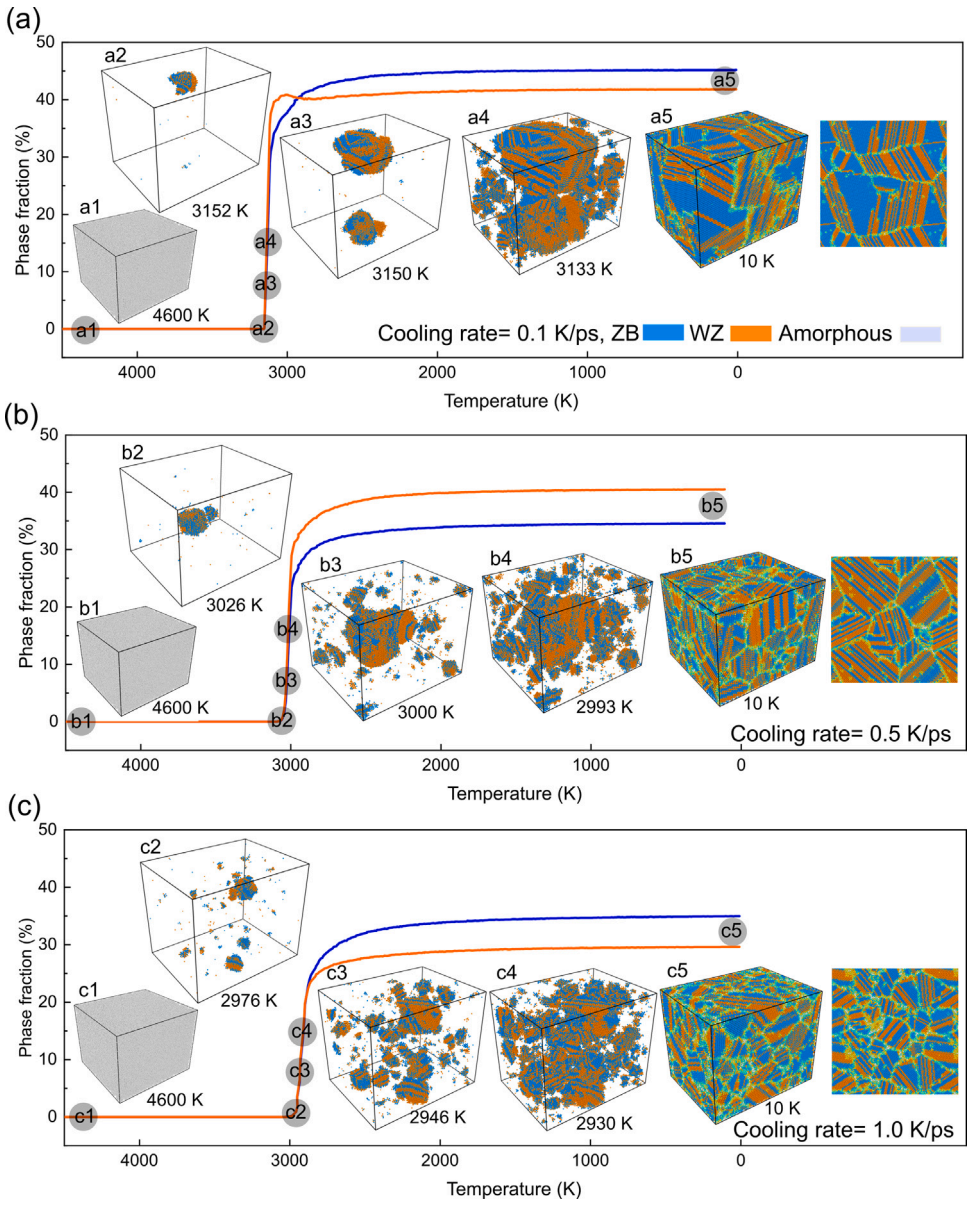

Fig. 1. Phase fraction analysis during the quenching process of GaN at cooling rates of (a) 0.1, (b) 0.5, and (c) 1 K/ps. The blue and orange curves display the fraction of ZB and WZ phases of GaN. The insets show the snapshots of phase distribution within the simulation domain. Blue and orange denote ZB phase and WZ phase, respectively, while white regions represent unidentifiable phase.

trends and assess how structural features (such as anisotropy, phase boundaries, twin boundaries, grain boundaries, and dislocations) impact thermal conductivity in melt-quenched GaN, particularly in the presence of coexisting defects.

3. Results and discussions

3.1. Microstructure evolution during quenching

Figs. 1a–c present the molecular dynamics simulation results of the quenching process of GaN at three different cooling rates: 0.1, 0.5, and 1 K/ps. Across all cases, significant nucleation of crystalline ZB and WZ phases occurs upon cooling. However, the onset temperature of crystallization and the resulting microstructure are notably influenced by the applied cooling rate, as discussed in detail below.

We first examine the slowest cooling case of 0.1 K/ps, as shown in Fig. 1a. The plot tracks the evolution of the volume fractions of ZB and WZ phases as the system cools. Insets a1–a4 provide representative snapshots of the atomic configuration, visualized using Identify Diamond Structure. Specifically, ZB and WZ regions are colored blue and orange, respectively, while defective regions are rendered transparent to better highlight the crystallization process.

At temperatures well above the melting point, the system exhibits fully disordered liquid behavior. Atoms undergo rapid, uncorrelated motion with no persistent ordering, as confirmed by the absence of any crystalline fraction and the homogeneous structure seen in inset a1. While transient clusters may form, thermal agitation dissolves them rapidly.

Upon cooling to approximately 3152 K, both ZB and WZ phases nucleate nearly simultaneously, reflected by a sharp increase in their volume fractions. This concurrent nucleation is attributed to the small cohesive energy difference between the two polymorphs. The first stable crystallite, observed in inset a2, consists of an interleaved ZB/WZ structure—essentially a ZB/WZ superlattice. Such dual-phase formation have been previously reported in both experimental studies [8] and MD

simulations [11], and they form naturally due to the minimal energetic difference of ~10 meV/atom between the two phases [12].

As the system continues to cool, multiple ZB/WZ composite nuclei form and expand into larger crystalline domains. At 3133 K (inset a4), the structure becomes substantially more crystalline, comprising approximately 14.7% ZB and 18.6% WZ phases. The remaining regions are still undergoing solidification and consist of liquid, amorphous solid, or interfacial areas such as phase and grain boundaries.

Below a characteristic temperature of 2900 K, the crystallization front stabilizes, and the system enters an annealing regime in which only minor structural changes occur. At the end of the quench (10 K), the final structure (inset a5) consists of well-defined ZB and WZ grains interspersed with structural defects, including twins and dislocations. Notably, the structure contains 45.2% ZB and 41.8% WZ phases, both in crystalline form. The remaining non-crystalline regions are primarily localized at ZB–WZ phase boundaries and grain boundaries. The nature and evolution of these defects formed during quenching will be discussed in a subsequent section.

Figs. 1b and 1c show the corresponding results for faster cooling rates of 0.5 K/ps and 1 K/ps. At a rate of 0.5 K/ps, the first stable nucleus emerges at approximately 3026 K (inset b2), while at the highest rate of 1 K/ps, nucleation is further delayed to around 2976 K (inset c2). In both cases, the initial nuclei adopt the same ZB/WZ superlattice motif as observed in the 0.1 K/ps case, but they form at progressively lower temperatures with increasing cooling rate.

This lower nucleation temperature reflects a greater degree of undercooling, which enhances the thermodynamic driving force for nucleation. Consequently, a larger number of nucleation sites emerge throughout the molten GaN, resulting in more crystalline grains. Sicne the total volume of the final, solidified GaN remains nearly constant, the increased number of grains means smaller average grain size. This trend is evident in the final structures shown in Figs. 1b5 and 1c5, which display more numerous and finer grains compared to the more coarsely grained structure in Fig. 1a5. The refinement in grain size with increasing cooling rate leads to a higher grain boundary density.

3.2. Nucleation cores and twinning of ZB/WZ superlattice structures

A prominent feature of the quenched GaN structures is the extensive presence of ZB/WZ superlattice-like phase domains. Detailed analysis of the nucleation events captured in our MD simulations reveals three distinct geometries for the nucleation core — spherical, tetrahedral, and diamond-shaped — resulting in three nucleation pathways, as illustrated in Fig. 2, to form ZB/WZ superlattice domains in GaN.

The most common nucleation motif involves a spherical ZB core, as shown in Fig. 2a. This process typically initiates with the formation of a small cluster of ZB GaN. Although the WZ phase is thermodynamically more stable in bulk GaN [32], prior studies suggest that ZB structures possess a lower nucleation energy barrier [13], likely due to their higher crystallographic symmetry. Early-stage nucleation of ZB clusters preceding WZ formation has also been reported in other III–V and II–VI semiconductors, such as ZnO, CdSe, CdTe [33–35].

As cooling proceeds, WZ layers nucleate heteroepitaxially on the ZB core, forming a sandwich-like ZB/WZ configuration. This behavior aligns with classical cross-nucleation theory, where one polymorph nucleates epitaxially on another with a small free energy difference [36, 37]. In GaN, the near-degeneracy in free energy between ZB and WZ phases [12] allows thermal fluctuations in the supercooled melt to overcome the nucleation barrier [38,39]. Additionally, the excellent crystallographic compatibility between ZB and WZ — specifically, $\{111\}_{ZB} \parallel \{0001\}_{WZ}$ and $\langle 110\rangle_{ZB} \parallel \langle 11\bar{2}0\rangle_{WZ}$ — promotes coherent heteroepitaxial nucleation with minimal interfacial energy.

The second nucleation motif involves a tetrahedral ZB core, as shown in Fig. 2b. This nucleus forms as a stable tetrahedron bounded by four equivalent {111} planes. The tetrahedral core remains structurally intact during cooling and serves as a rigid seed for the subsequent epitaxial growth of WZ layers. As temperature decreases, WZ layers nucleate coherently on each of the tetrahedron's faces, resulting in four distinct ZB/WZ superlattice domains oriented along the normals of the tetrahedral faces. Compared to the spherical core, which typically gives rise to a single superlattice, the tetrahedral core facilitates the formation of a superlattice cluster with multiple growth directions. This behavior mirrors the formation of tetrapod-shaped ZnO and ZnS nanowires, where ZB tetrahedra serve as cores for WZ leg growth [33, 34].

Subsequently, as shown in the last snapshot of Fig. 2b, a twin forms between two legs of a tetrahedral nucleation core. The orientation relationship between these legs closely resembles the $\{10\bar{1}3\}$ twin as previously reported in ZnO nanowires, where pure WZ legs nucleate from a ZB core [34]. In contrast, our simulations reveal that the legs are composed of ZB/WZ superlattice structures rather than pure WZ.

The third observed motif is a diamond-shaped nucleus formed by the coalescence of two mirrored ZB tetrahedra sharing a common {111} plane (Fig. 2c), providing multiple {111} facets that act as low-energy sites for subsequent epitaxial growth of ZB/WZ superlattice layers. The growth mechanism is analogous to that observed in the single tetrahedral case but offers additional facets for crystal growth and superlattice expansion.

Additionally, the last snapshot of Fig. 2c shows that as the superlattice structures grow outward along the legs of the diamond-shaped core, they maintain this twin symmetry between neighboring superlattice domains. Moreover, it is interesting to note the two tetrahedra forming the diamond-like core form a {111} twin relationship.

In all three nucleation pathways, the ZB phase consistently initiates the process, followed by coherent heteroepitaxial growth of WZ layers. The repeated involvement of crystallographically aligned planes, coupled with the nearly identical free energies of the two phases, facilitates cooperative nucleation and stabilizes the formation of intricate ZB/WZ superlattice architectures. Functionally, these twin between different superlattice domains act as grain boundaries separating distinct superlattice domains.

3.3. Dislocations and stacking faults

Dislocations and stacking faults are frequently observed in melt-quenched materials. In this section, we examine the evolution of these crystal defects during the quenching process and investigate how their formation and transformation depend on the cooling rate.

3.3.1. Dislocations

Extensive dislocation formation is observed in the melt-quenched GaN structures obtained from our simulations. Fig. 3a shows the evolution of dislocation density during quenching at a cooling rate of 0.1 K/ps, as analyzed using the Dislocation Extraction Algorithm (DXA) implemented in OVITO [40]. The DXA analysis reveals the formation of several dislocation types, including $1/6\langle 112\rangle$ Shockley, $1/2\langle 110\rangle$ Perfect, $1/6\langle 110\rangle$ Stair-rod, and $1/3\langle 111\rangle$ Frank dislocations. Dislocation-like defects that do not match these classifications are labeled as "Other". Fig. 3f demonstrates that "Other" dislocations are formed mostly in grain boundary regions, thus it can serve as an approximate measure of the amount of grain boundaries in the structure.

At temperatures above the nucleation point (3152 K), the system is fully molten and exhibits no dislocation activity (Fig. 3b). As the temperature drops and the first nuclei emerge, a sudden increase in the density of $1/6\langle 112\rangle$ Shockley (green curve) and "Other (or grain boundaries)" (red curve) is observed (Fig. 3a). This jump coincides with the onset of solidification, where both ZB and WZ phases begin to form, thus leading to more Shockley dislocations, and the nucleation and growth of grains leads to more grain boundaries. As nucleation progresses and crystalline grains grow, various types of dislocations develop and expand throughout the polycrystalline structure (Fig. 3e). Among all observed dislocations, $1/6\langle 112\rangle$ Shockley

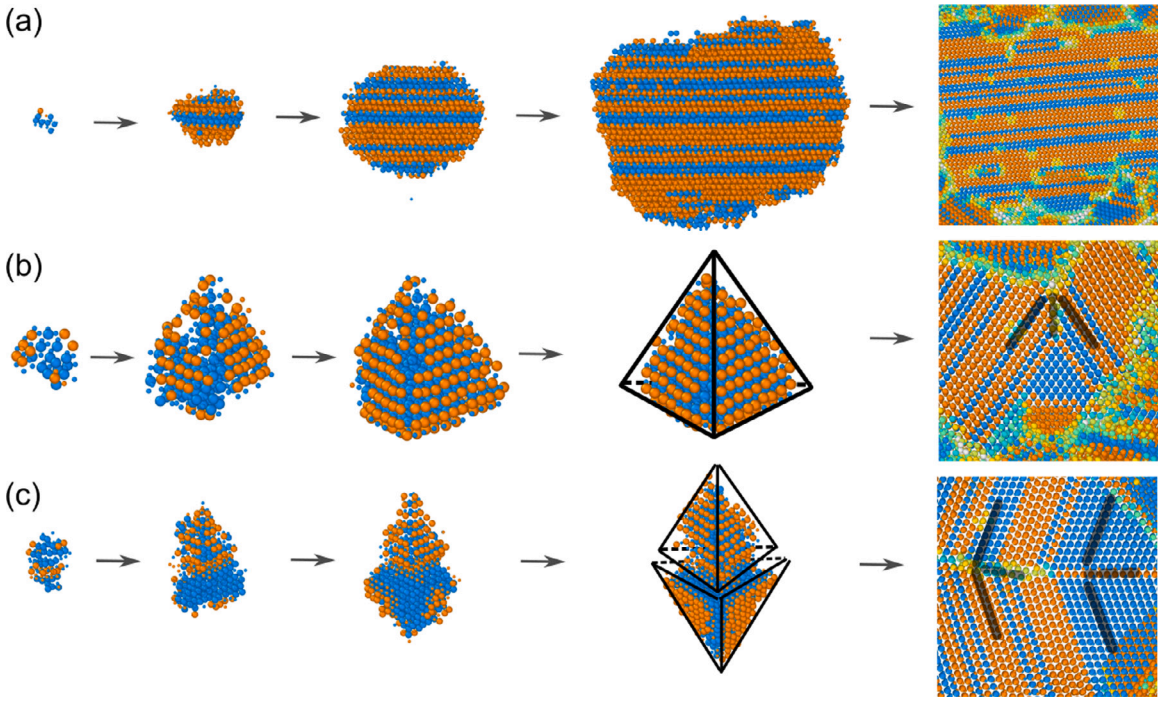

Fig. 2. Nucleation process of three representative nucleation motifs observed during the early stages of ZB/WZ superlattice formation in GaN: (a) spherical ZB core with heteroepitaxial WZ layers; (b) tetrahedral ZB core with WZ growth on three {111} facets; (c) diamond-shaped core formed by coalesced twin tetrahedra, serving as a multifaceted template for ZB/WZ superlattice growth. The last snapshot of each panel shows the final, large-scale superlattice or twinned superlattice structure after growth from the corresponding nucleation core.

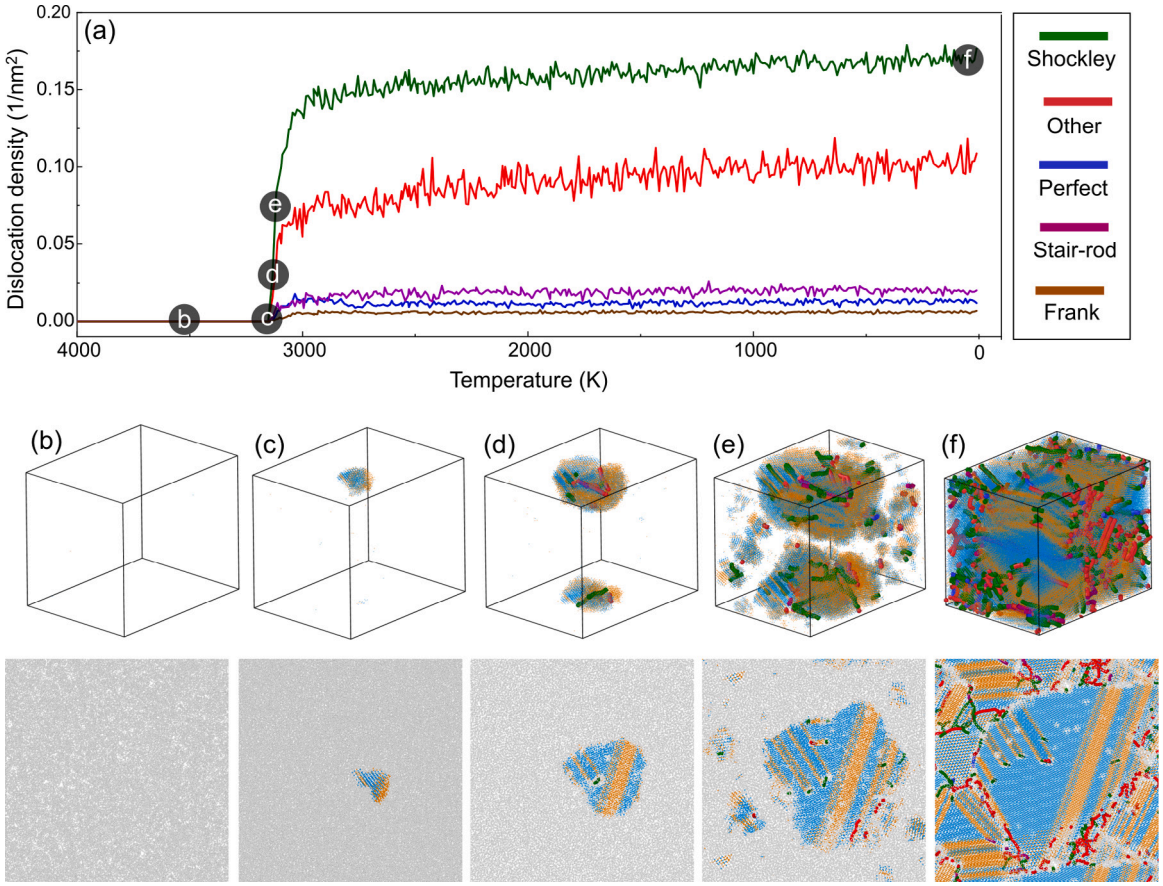

Fig. 3. Evolution of dislocation density during the quenching process at a cooling rate of 0.1 K/ps. Panels (b)–(f) show dislocation distributions at selected temperatures (3500 K, 3152 K, 3150 K, 3133 K, and 10 K) indicated in panel (a).

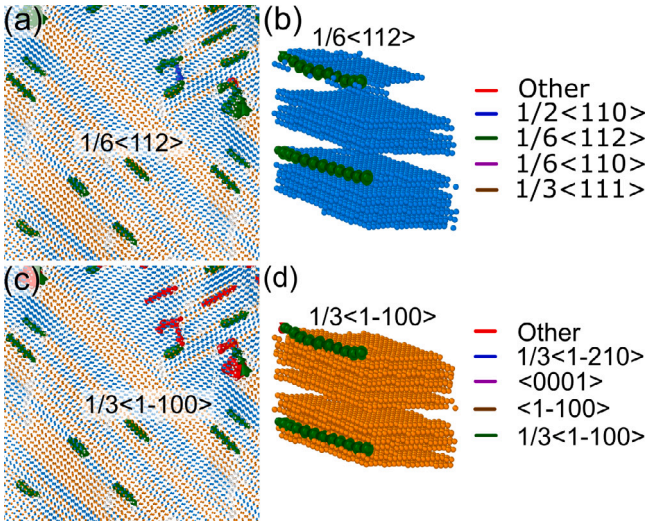

Fig. 4. The quenched microstructure at the cooling rate of 0.1 K/ps with dislocation analysis using ZB and WZ as the references. (a) and (b) 2D and 3D microstructure using ZB as the reference structure. (c) and (d) 2D and 3D microstructure using WZ as the reference structure. The top and bottom rows represent the same regions for direct comparison.

dislocations (green) are the most prevalent, followed by "Other" (red), Perfect (blue), Stair-rod (purple), and Frank (brown) dislocations. As shown in Fig. 3f, many of these defects originate at grain boundaries and phase interfaces. Notably, Shockley dislocations predominantly reside within grains rather than along boundaries, indicating that they are likely associated with stacking faults or phase interfaces within the grains.

To further understand the nature of Shockley dislocations, we analyze the largest grain in the quenched structure at 0.1 K/ps (Fig. 3f). As shown in Fig. 4a, Shockley dislocations are predominantly located at the interfaces between ZB and WZ phases in the superlattice-like ZB/WZ microstructure. To isolate these dislocations more clearly, we remove the ZB atoms from the visualization. The resulting WZ-focused microstructure(Fig. 4b) reveals that Shockley dislocation lines are concentrated along the ZB/WZ interfaces. This confirms that the Shockley dislocations are intrinsic features of the ZB/WZ phase boundaries, in agreement with prior studies on stacking fault and dislocation formation in semiconductor superlattices [41,42].

Because the DXA method requires a reference crystalline structure, we conduct parallel analyses using both ZB and WZ as references. While the primary discussion above employs the ZB structure as the reference — owing to the broader understanding of dislocation types in cubic systems — we perform a complementary analysis using the WZ structure to ensure the robustness of our interpretation.

As shown in Figs. 4d–f, DXA using the WZ reference identifies additional dislocation types, including $1/3\langle 1\bar{2}10\rangle$, $\langle 0001\rangle$, $\langle 1\bar{1}00\rangle$, and $1/3\langle 1\bar{1}00\rangle$ dislocations, along with unclassified defects ("Other"). Each of these WZ-identified dislocations has a one-to-one correspondence with the dislocations previously identified using the ZB reference. For example, the $1/3\langle 1\bar{1}00\rangle$ dislocation identified in WZ maps precisely to the $1/6\langle 112\rangle$ Shockley dislocation identified using ZB. Similar correspondence is observed between $1/3\langle 1\bar{2}10\rangle$ perfect dislocation in WZ and $1/2\langle 110\rangle$ perfect dislocation in ZB. These results confirm that both reference systems capture the same underlying dislocation network, thereby validating the structural interpretation.

To elucidate the impact of cooling rate on dislocation formation, we examine the results from the faster quenching cases (0.5 and 1.0 K/ps), as shown in Fig. 5. As in the 0.1 K/ps case, the dislocation density rises sharply during solidification, followed by a gradual increase as the system cools further, as expected for the annealing process. Across all cooling rates, Shockley dislocations remain the dominant type. A key difference among the three cases lies in the onset temperature of dislocation formation: higher cooling rates delay the onset of both solidification and dislocation nucleation, consistent with the enhanced undercooling discussed in Section 3.1.

A particularly notable feature emerges in the evolution of $1/2\langle 110\rangle$ Shockley dislocations (green curve) for the 0.5 K/ps case, shown in Fig. 5a. Immediately following the abrupt increase associated with solidification, the Shockley dislocation density steadily decreases as the temperature drops to 2500 K. Simultaneously, the density of $1/2\langle 110\rangle$ perfect dislocations (blue curve) gradually increases. This inverse trend is not coincidental, but rather indicative of a dislocation reaction mechanism in which Shockley partials recombine to form perfect dislocations.

Such behavior is negligible at the slower 0.1 K/ps cooling rate (Fig. 3a), where the density of perfect dislocations remains low. In contrast, it becomes prominent in the faster cooling cases (Figs. 5a and 5b), where the density of perfect dislocations reaches nearly half or one third that of Shockley dislocations. This enhanced recombination can be attributed to the finer grain sizes at higher cooling rates, which increase the likelihood of Shockley partials encountering one another — especially at ZB/WZ phase boundaries — thus facilitating the formation of perfect dislocations.

Furthermore, the total dislocation density in the final quenched structure shows a pronounced dependence on cooling rate. As summarized in Fig. 5c, the density of Shockley dislocations decreases significantly with increasing cooling rate, reflecting the diminished development of well-ordered ZB/WZ superlattice regions due to the restricted grain growth. In contrast, the density of $1/2\langle 110\rangle$ perfect dislocations increases with cooling rate.

Taken together, these findings underscore the sensitivity of dislocation structures in melt-quenched GaN to the cooling rate. Faster quenching results in higher levels of crystalline imperfection, reduced phase ordering, and increased structural disorder, which are closely linked to both grain refinement and interfacial interactions during rapid solidification.

3.3.2. *Stacking faults*

Stacking faults constitute a common class of planar defects that are essentially local disruptions in the regular stacking sequence of atomic planes. In the quenched GaN structures investigated in this work, stacking faults are observed in both ZB- and WZ-dominant regions. These faults originate from growth irregularities (faults), resulting in local intermixing of ZB and WZ layers. Given the small energy difference between the two phases, the high quenching rate promotes their coexistence, leading to frequent phase intergrowth and the emergence of stacking faults.

Fig. 6 illustrates the various stacking faults observed in WZ structures. The ideal WZ phase exhibits an ABABAB stacking sequence oriented along the **c**-axis ($\langle 0001\rangle$ direction), where each layer (A or B) represents a basal layer containing a two-atom basis of Ga and N atoms. The C position represents a third possible basal layer site that is not occupied in the WZ structure. Four types of intrinsic stacking faults are identified in WZ structures, labeled as Intrinsic I, II, III, and Extrinsic SFs [43]. It should be noted that the stacking faults formed during the quenching process must be bounded by misfit dislocations or end at grain boundaries.

While the stacking faults in the melt-quenched GaN in this work are growth faults, in the following discussions, we will elucidate their structure, particularly the stacking sequence and displacement vector, by making an analogy with the stacking faults formed through dislocation slip in fcc and hcp crystals.

The Intrinsic I stacking fault is formed through the growth of a single ZB layer within the WZ matrix. It is the energetically most favorable type among all four types of stacking faults shown in Fig.

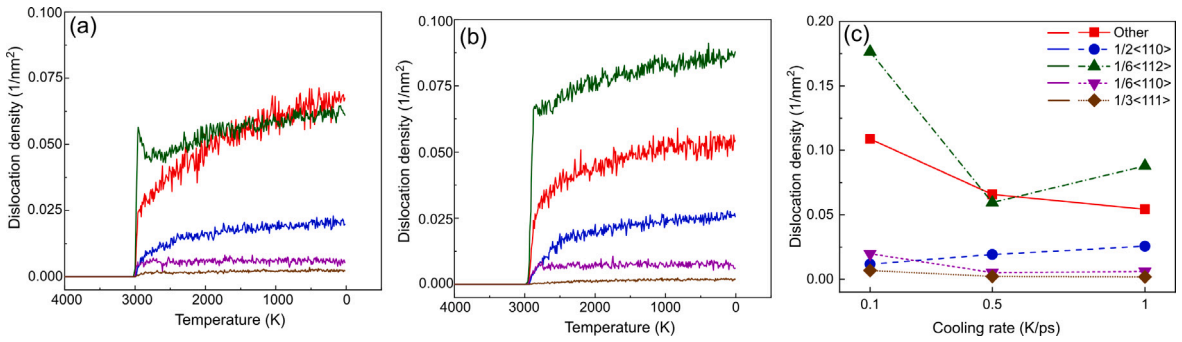

Fig. 5. (a, b) Evolution of dislocation density during quenching at cooling rates of 0.5 K/ps and 1.0 K/ps, respectively. (c) Final dislocation densities in quenched GaN as a function of cooling rate for various dislocation types.

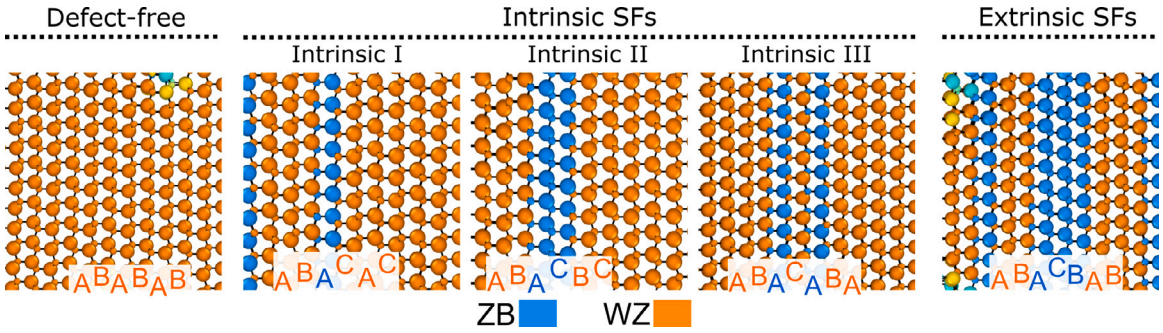

Fig. 6. Stacking faults in the WZ structure. Gold regions indicate the WZ phase, while blue regions indicate ZB layers. The ideal WZ phase exhibits an ABABAB stacking sequence oriented along the **c**-axis (⟨0001⟩ direction), where each layer (A or B) corresponds to a basal plane containing a two-atom basis of Ga and N. The C position represents a third possible basal layer site that is not occupied in the WZ structure.

6. Specifically, the stacking sequence of the Intrinsic I stacking fault is AB-**A**-CACA. Such a stacking sequence agrees with the I_1 stacking fault in the hcp lattice, which is equivalent to removing a basal layer, followed by a subsequent slip of a partial dislocation with a Burgers vector of $b_p = 1/3\langle 10\bar{1}0\rangle$ [44,45]. Therefore, the resulting displacement vector for the Intrinsic I stacking fault is $\mathbf{b_p} + \frac{1}{2}\mathbf{c} = 1/6\langle 20\bar{2}3\rangle$.

Intrinsic II stacking faults, in contrast, form through the growth of two ZB layers within the WZ matrix. As shown in Fig. 6, their stacking sequence is AB-**AC**-BCBC. This stacking sequence is analogous to the stacking faults induced by the glide of a Shockley partial dislocation with a Burgers vector of $1/3\langle 10\bar{1}0\rangle$ in hcp materials [46]. The only difference is that WZ has a pair of Ga and N atoms that corresponds to a single atom in hcp materials. Thus, the resulting displacement vector is equal to $b_p = 1/3\langle 10\bar{1}0\rangle$.

The Intrinsic III stacking fault is formed by the growth of two ZB layers, separated by a single WZ layer in the middle, within the WZ matrix. As shown in Fig. 6, its stacking sequence is AB-**A**-C-**A**-BABA. The Intrinsic III stacking fault can be viewed as being bounded by two partial dislocation slips of $1/3\langle 10\bar{1}0\rangle$ in adjacent basal planes [44]. Accordingly, the corresponding displacement vector is $2\mathbf{b_p}$, and its energy lies between those of Intrinsic I and Intrinsic II [44,45].

Finally, the extrinsic stacking fault consists of the growth of three ZB layers within the WZ matrix. Its stacking sequence is determined to be AB-**ACB**-AB, as shown in Fig. 6. Compared to the ideal ABABAB stacking sequence in WZ, this stacking fault can form through the accidental growth of an extra C basal layer in the original WZ stacking sequence. Thus, its displacement vector is $\frac{1}{2}\mathbf{c}$. Such extrinsic stacking faults are much rarer than intrinsic ones in the WZ structure because their formation requires overcoming a high energy barrier [44].

Stacking faults are also prominent in regions dominated by the ZB structure. The stacking sequence or faults in ZB structures are structurally analogous to those observed in face-centered cubic materials. As shown in Fig. 7, the perfect ZB structure is characterized by an

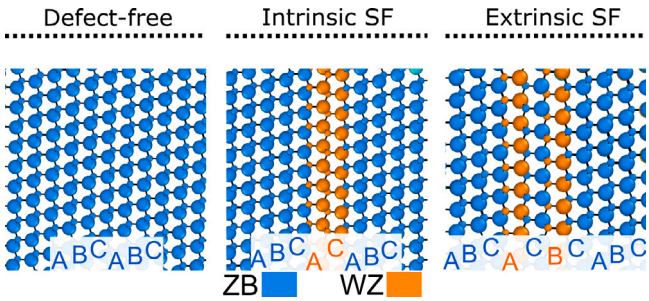

Fig. 7. Stacking faults in the ZB structure. Blue atoms indicate the ZB phase, while gold atoms indicate WZ layers. The ideal ZB phase exhibits an ABCABCABC stacking sequence oriented along the ⟨111⟩ direction, where each A, B, or C layer corresponds to a close-packed plane containing a two-atom basis of Ga and N.

ABCABC stacking sequence. Stacking faults in this phase appear as local deviations from this sequence and can be classified as intrinsic or extrinsic.

Intrinsic stacking faults in the ZB structure are formed through the growth of two WZ layers within the ZB matrix. As shown in Fig. 7, the corresponding stacking sequence is ABC-**AC**-ABC. In the fcc lattice, this sequence reflects the absence of a B layer and can be introduced by the glide of a single Shockley partial dislocation [47,48]. Correspondingly, the displacement vector for the intrinsic SF is $1/6\langle 1\bar{1}2\rangle$.

In contrast to intrinsic stacking faults, an extrinsic stacking fault consists of two WZ layers separated by one ZB layer, yielding an ABC-**A**-C-**B**-CABC stacking sequence, as illustrated in Fig. 7. In the fcc lattice, this pattern corresponds to the insertion of an extra C layer into the ideal ABCABCABC stacking. As shown by Tian et al. [47], this fault can be formed through the sequential glide of two Shockley dislocations in

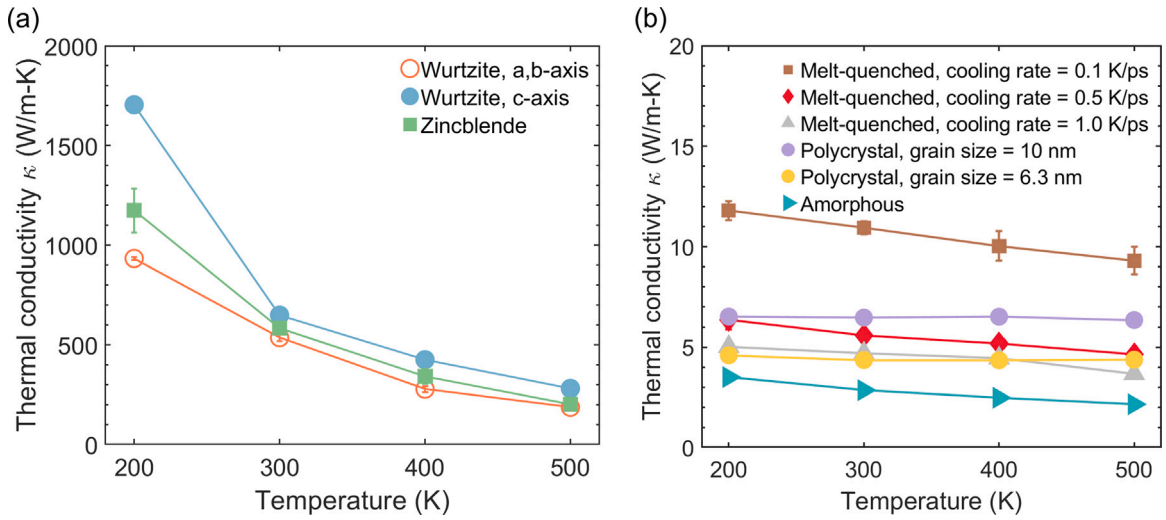

Fig. 8. Temperature-dependent thermal conductivity κ of (a) pristine WZ and ZB GaN crystals and (b) melt-quenched GaN samples obtained at different cooling rates, artificially constructed polycrystalline WZ GaN with varying grain sizes, and amorphous GaN.

scenarios involving significant dislocation activity, while it is formed through a growth fault in our melt-quenching simulations. Accordingly, the displacement vector for the extrinsic SF is $1/3\langle 1\bar{1}2\rangle$.

3.4. Lattice thermal transport properties

3.4.1. Melt-quenched GaN and nanograined GaN

To gain insight into thermal transport in the melt-quenched GaN structures with complex microstructural features discussed in Section 3.1, we first examine the baseline thermal conductivity, κ, of pristine ZB and WZ GaN crystals. Fig. 8a shows the temperature-dependent κ values predicted from EMD simulations. As expected, WZ GaN exhibits notable anisotropy due to its hexagonal lattice structure. Specifically, κ along the c-axis is significantly higher than that along the a- and b-axes. In contrast, ZB GaN displays isotropic κ, consistent with its cubic symmetry. Notably, ZB GaN has higher κ than WZ GaN along the a/b axes but lower κ than WZ GaN along the c-axis, with this difference becoming more prominent at lower temperatures.

Although a full phonon-level analysis is beyond the scope of this work, it is worth highlighting that literature reports diverge regarding both the magnitude and anisotropy of κ in WZ GaN. For instance, Lindsay et al. [49] predicted higher κ along the a/b directions based on first-principles calculations, while Monte Carlo simulations from Luo et al. [50], incorporating full phonon dispersion, suggested the c-axis has higher κ. Experimental studies by Zheng et al. [51], using time-domain thermoreflectance (TDTR), showed only weak anisotropy. Similarly, Tran et al. [52] employed both thermoreflectance measurements and Boltzmann transport equation (BTE) simulations under the relaxation time approximation. Their experiments revealed minor anisotropy over a wide temperature range, while their BTE analysis showed higher κ along a/b below 300 K, transitioning toward isotropy at elevated temperatures. Despite these discrepancies, the consensus is that anisotropy in WZ GaN is modest, and differences among reports largely arise from the treatment of phonon scattering—whether via relaxation-time approximations or full iterative solutions to the BTE.

While the Stillinger–Weber potential employed in our simulations was not explicitly parameterized for phonon transport, it successfully captures key qualitative trends, such as the anisotropy of WZ GaN and the temperature dependence of κ. Furthermore, the predicted values are in reasonable agreement with experimental data, supporting the potential's suitability for the current study. Nevertheless, we note that future work using machine learning potentials trained on high-fidelity quantum data, such as those developed in recent studies [53–57], could offer enhanced accuracy and transferability, especially for disordered and defect-rich structures of various materials.

Fig. 8b presents the thermal conductivity of melt-quenched GaN samples obtained under varying cooling rates. At 300 K, κ ranges from approximately 4 to 12 W/m K, representing a dramatic 97%–99% reduction from that of pristine crystals shown in Fig. 8a. This substantial suppression underscores the promise of ultrafast melt-quenching as a strategy for engineering low-κ materials for thermoelectric and thermal barrier applications.

The results clearly indicate that κ decreases with increasing cooling rate. Faster cooling yields smaller grains and higher defect densities, as discussed in Section 3.1, which intensify grain boundary scattering of phonons and suppress phonon heat conduction. The influence of ZB/WZ superlattice regions on thermal transport will be examined further in the following subsection.

Interestingly, all melt-quenched samples exhibit a mild reduction in κ with increasing temperature. The slowest quenched sample (0.1 K/ps), which is the most crystalline, shows the most pronounced temperature dependence. This behavior is characteristic of crystalline materials, where anharmonic phonon–phonon scattering intensifies with temperature [58,59]. In contrast, heavily disordered materials or materials containing a high density of interfaces typically exhibit increasing κ with temperature due to enhanced inelastic phonon transmission across structural interfaces or increased hopping of localized vibrational modes [60–64].

To further assess the role of grain boundaries, we constructed nanograined WZ GaN models using Voronoi tessellation with average grain sizes of 10 nm and 6.3 nm. As shown in Fig. 8b, the 10 nm grain model exhibits higher κ than the 6.3 nm case, whose κ drops to approximately 4–5 W/m K, which is comparable to that of the fastest-quenched (1 K/ps) melt-quenched sample. These results provide direct evidence that phonon scattering at grain boundaries is the primary limiting factor for thermal transport in melt-quenched GaN. Increasing the density of grain boundaries, whether through rapid quenching or intentional nanostructuring, substantially reduces κ, making these structures highly promising for thermal insulation and energy conversion applications.

3.5. Superlattice-like ZB/WZ GaN structures

Superlattices, particularly those with aperiodic or disordered layer thicknesses, are known to exhibit markedly reduced thermal conductivities compared to their bulk counterparts [65–68]. This observation

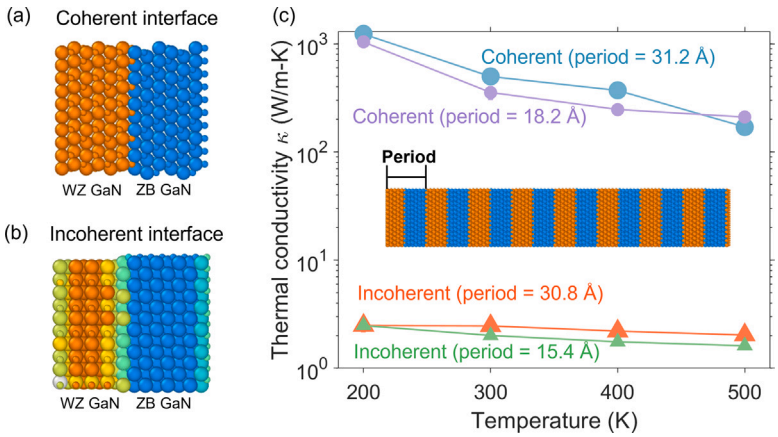

Fig. 9. Comparison of thermal conductivity κ in WZ GaN/ZB GaN superlattices with coherent and incoherent interfaces. (a) A coherent interface formed by aligning the [0001] direction of WZ GaN (orange) with the [111] direction of ZB GaN (blue). (b) An incoherent interface formed at arbitrary crystallographic orientations. (c) Cross-plane temperature-dependent thermal conductivity κ of superlattices with coherent and incoherent interfaces, obtained from EMD simulations.

naturally motivates the hypothesis that the superlattice-like domains comprising ZB and WZ GaN in melt-quenched samples could be key contributors to the suppressed thermal conductivity κ. However, as we demonstrate in this section, these domains can retain relatively high κ values, approaching those of pristine crystals, depending strongly on the nature of the interfacial structure.

Before presenting our simulation results, we highlight a critical crystallographic feature: WZ GaN and ZB GaN possess nearly identical local bonding environments, with the primary difference being their stacking sequences. Specifically, WZ GaN follows an ABAB sequence along the [0001] direction, whereas ZB GaN exhibits an ABCABC sequence along the [111] direction. When these two phases interface with the [0001] direction of WZ GaN aligned to the [111] direction of ZB GaN, atomically coherent phase boundaries can form, as illustrated in Fig. 9a. These coherent interfaces are energetically favorable and commonly arise during the rapid solidification of GaN. In contrast, incoherent interfaces, which are formed when the phases meet at arbitrary crystallographic orientations, are also possible and are shown in Fig. 9b.

To assess the effect of interface coherence on thermal transport, we perform EMD simulations on ZB/WZ GaN superlattices featuring both coherent and incoherent interfaces. Two average layer thicknesses, 31.2 Å and 18.2 Å, are considered to evaluate the dependence of κ on period length, a crucial factor known to significantly affect phonon transport in superlattice structures.

As shown in Fig. 9c, superlattices with coherent interfaces maintain high cross-plane thermal conductivities, on the order of ~300 W/m K, which are only 20%–30% lower than that of pristine WZ or ZB GaN crystals. This is in stark contrast to prior reports of both periodic and aperiodic superlattices, where thermal conductivity reductions of 70% or more have been observed [66,69,70], and in extreme cases, reductions approaching 95% have been reported [29,67]. Some aperiodic superlattices have even demonstrated thermal conductivities below the effective alloy limit, approaching those of amorphous solids [29].

In contrast, ZB/WZ GaN superlattices with incoherent interfaces show a dramatic suppression in κ, with values ranging from 1 to 2 W/m·K, which are significantly lower than even the melt-quenched GaN samples discussed previously. Furthermore, the thermal conductivity of these incoherent-interface superlattices exhibits a strong dependence on period length, underscoring the dominant role of interface scattering in limiting phonon transport.

To gain deeper insight into the underlying mechanisms, we calculated the interfacial thermal resistance (R_I) of individual interfaces using NEMD simulations, as described in Section 2. The examined interfaces include coherent and incoherent ZB/WZ phase boundaries, as well as representative grain boundaries in both WZ and ZB GaN.

Table 1 summarizes the extracted R_I values from our simulations. The coherent ZB/WZ interface exhibits an exceptionally low thermal resistance of 1.08×10^{-10} m^{2}K/W, over an order of magnitude lower than that of the incoherent interface (1.35×10^{-9} m^{2}K/W) and markedly lower than those of all grain boundary types. Remarkably, this value is also one to two orders of magnitude smaller than the typical interfacial resistances reported for conventional material systems such as Cu/diamond [71] and Si/Ge [72], as predicted by molecular dynamics simulations.

To further elucidate the influence of interface coherence on thermal transport across ZB/WZ interfaces, we decomposed the interfacial thermal conductance (i.e., the inverse of R_I) into frequency-dependent contributions following the approach of Refs. [61]. As shown in Fig. 10a, the conductance across all phonon frequency ranges is substantially suppressed for the incoherent ZB/WZ interface compared with the coherent one. Fig. 10b presents the vibrational density of states (vDOS), calculated from the Fourier transform of atomic velocity–velocity autocorrelation functions using velocity data obtained from equilibrium MD simulations. Evidently, the vDOS profiles of the ZB and WZ phases are highly similar—the differences are far less pronounced than those observed in the thermal conductance spectra in Fig. 10a. This indicates that the pronounced and broadband reduction in $G(\omega)$ for the incoherent interface does not stem from vibrational spectrum mismatch, which typically dominates the Kapitza resistance at interfaces between dissimilar materials, as described by the conventional acoustic and diffuse mismatch models [59,73], nor the need for redistributing heat flux at the interface [64]. Instead, the elevated R_I and suppressed $G(\omega)$ of the incoherent ZB/WZ interface primarily originate from its insufficient (weakened) and incoherent atomic bonding [74].

The ultralow R_I of the coherent ZB/WZ interface can be attributed to two main factors: (1) the atomically smooth and structurally coherent nature of the interface, stemming from the minimal mismatch between the two phases, which differ only in their stacking sequence perpendicular to the interface; and (2) the highly similar phonon dispersion relations of WZ and ZB GaN, as shown in Fig. 11, which facilitate efficient phonon transmission across the interface. These features collectively enable coherent interfaces to maintain high thermal conductivities, in contrast to the severe phonon scattering encountered at incoherent boundaries.

4. Conclusion

In this study, we conducted a comprehensive investigation of the microstructural evolution and thermal transport properties of GaN

Table 1
Interfacial thermal resistance (R_I) for representative interfaces in melt-quenched GaN. The third column presents the R_I of each interface normalized by that of the coherent ZB/WZ phase boundary. Coherent interfaces exhibit the lowest thermal resistance that is an order of magnitude lower than that of grain boundaries or incoherent interfaces.

Interface type	R_I ($\times 10^{-9}$ m^{2}K/W)	Relative R_I ($R_I/R_{I,\text{coh-ZB/WZ}}$)
Coherent ZB/WZ phase boundary	0.11	1.0
Incoherent ZB/WZ phase boundary	1.35	12.3
Grain boundary within WZ GaN	0.79	7.2
Grain boundary (type 1) within ZB GaN	0.85	7.7
Grain boundary (type 2) within ZB GaN	1.20	10.9
Grain boundary (type 3) within ZB GaN	0.82	7.5

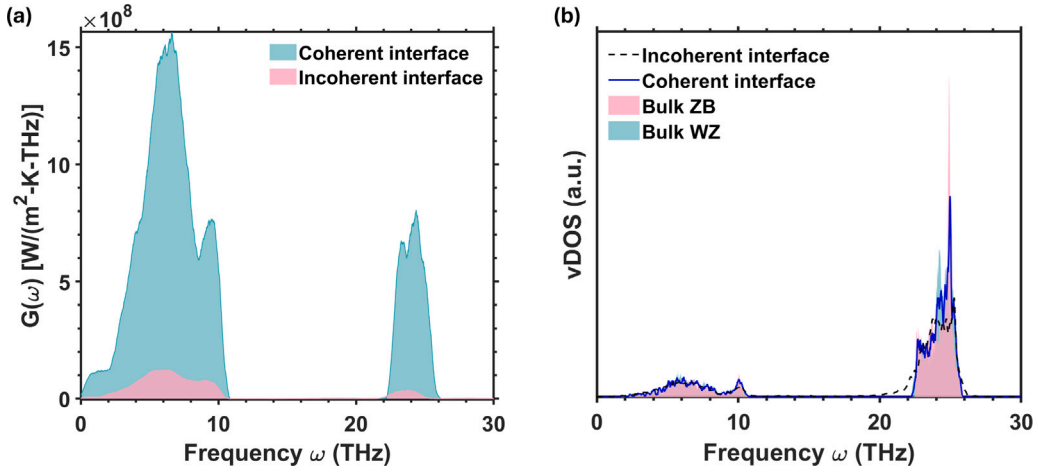

Fig. 10. (a) Comparison of the interfacial thermal conductance spectra $G(\omega)$ for the coherent and incoherent ZB/WZ interfaces. (b) Comparison of the vDOS of bulk ZB GaN and bulk WZ GaN, along with the vDOS calculated for the interfacial regions of the coherent and incoherent ZB/WZ interfaces.

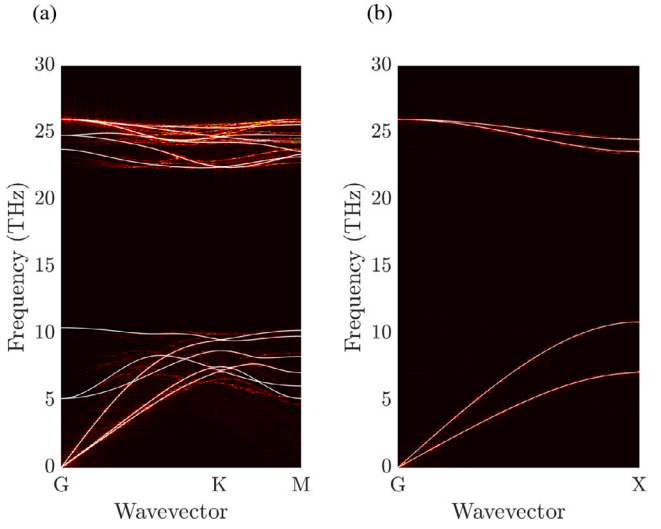

Fig. 11. Phonon dispersion relations of WZ GaN and ZB GaN obtained from phonon spectral energy density (SED) analysis in EMD simulations, following the same procedure in Ref. [75]. A 1.2 by 2.2 by 62.3 nm^3 supercell was used in the SED calculation of WZ GaN and 1.8 by 1.8 by 54 nm^3 supercell was used for ZB GaN. The similarity in phonon spectra supports efficient phonon transmission across the coherent interface.

under ultrafast quenching, using classical molecular dynamics simulations. By systematically varying cooling rates, we elucidated the nucleation and growth mechanisms that give rise to complex crystalline domains, including ZB, WZ, and ZB/WZ superlattice structures. Our results demonstrate that higher cooling rates suppress nucleation, promote undercooling, and lead to the formation of finer grains with increased structural disorder due to restricted atomic mobility.

A key finding is the identification of three characteristic nucleation core geometries (i.e., spherical, tetrahedral, and diamond-shaped) that serve as precursors for ZB/WZ superlattice formation. These structures evolve through heterogeneous epitaxial growth of WZ layers on ZB cores, driven by the minimal free energy differences and crystallographic compatibility between the two phases. The resulting microstructures exhibit a rich variety of defects, including twins, stacking faults, and multiple dislocation types. Twinning occurs both within ZB regions and across ZB/WZ superlattice domains, while stacking faults are prominent in both ZB- and WZ-rich regions. Dislocation analysis reveals the presence of mostly Shockley and perfect dislocations, whose densities and types depend strongly on the local phase and thermal history.

We further examined the impact of these microstructures on phonon-mediated thermal transport. Quenched GaN, characterized by nanoscale grains, phase boundaries, and a high density of dislocations, exhibits ultralow lattice thermal conductivities, i.e., up to 99% lower than that of pristine GaN. This dramatic reduction is primarily attributed to enhanced phonon scattering at grain boundaries, a conclusion supported by additional simulations of nanograined WZ-GaN models. These results underscore the significant tunability of GaN thermal transport via ultrafast melt-quenching and nanoscale microstructural engineering.

Interestingly, we find that coherent WZ-GaN/ZB-GaN interfaces retain relatively high thermal conductivity, approaching bulk values. This behavior contrasts with prior superlattice-based expectations and is attributed to the atomically smooth, coherent interfaces and strong phonon mode matching across the boundary. In contrast, incoherent phase boundaries lead to a substantial thermal conductivity reduction, with values as low as 1–2 W/m K, lower even than those of melt-quenched structures. Non-equilibrium molecular dynamics simulations

further show that the interfacial thermal resistance of coherent WZ-GaN/ZB-GaN boundaries is orders of magnitude lower than that of incoherent boundaries and grain interfaces.

Overall, this work provides atomistic insights into solidification dynamics, defect formation, and polymorph coexistence in GaN under non-equilibrium conditions. These findings not only deepen our understanding of the thermal behavior of laser-melt-quenched GaN but also offer practical guidance for tailoring thermal transport in GaN-based devices through controlled microstructure design.

CRediT authorship contribution statement

Mehrab Lotfpour: Writing – review & editing, Writing – original draft, Methodology, Investigation. **Haoran Cui:** Writing – review & editing, Writing – original draft, Methodology, Investigation. **Nolan Hagen:** Writing – review & editing, Writing – original draft, Methodology, Investigation. **Milad Nasiri:** Writing – review & editing, Writing – original draft, Methodology, Investigation. **Theodore Maranets:** Writing – review & editing, Writing – original draft, Methodology, Investigation. **Yan Wang:** Writing – review & editing, Writing – original draft, Supervision, Project administration, Methodology, Investigation. **Lei Cao:** Writing – review & editing, Writing – original draft, Supervision, Project administration, Methodology, Investigation.

Declaration of competing interest

The authors declare that they have no known competing financial interests or personal relationships that could have appeared to influence the work reported in this paper.

Acknowledgments

This work is supported by the National Science Foundation, United States (Award No. CBET-1953300). Additionally, the authors would like to acknowledge the support provided by the Research and Innovation team and the Cyberinfrastructure Team in the Office of Information Technology at the University of Nevada, Reno, for facilitating access to the Pronghorn High-Performance Computing Cluster.

Data availability

Data will be made available on request.

References

[1] S. Rajbhandari, J.J. McKendry, J. Herrnsdorf, H. Chun, G. Faulkner, H. Haas, I.M. Watson, D. O'Brien, M.D. Dawson, A review of gallium nitride LEDs for multi-gigabit-per-second visible light data communications, Semicond. Sci. Technol. 32 (2) (2017) 023001.
[2] A. Udabe, I. Baraia-Etxaburu, D.G. Diez, Gallium nitride power devices: A state of the art review, Ieee Access 11 (2023) 48628–48650.
[3] S.N. Mohammad, A.A. Salvador, H. Morkoc, Emerging gallium nitride based devices, Proc. IEEE 83 (10) (1995) 1306–1355.
[4] H.W. Seo, S.Y. Bae, J. Park, H. Yang, K.S. Park, S. Kim, Strained gallium nitride nanowires, J. Chem. Phys. 116 (21) (2002) 9492–9499.
[5] K. Zhang, Y. Dai, Z. Zhou, S.U. Jan, L. Guo, J.R. Gong, Polarization-induced saw-tooth-like potential distribution in Zincblende-Wurtzite superlattice for efficient charge separation, Nano Energy 41 (2017) 101–108.
[6] R.E. Algra, M.A. Verheijen, M.T. Borgström, L.-F. Feiner, G. Immink, W.J. van Enckevort, E. Vlieg, E.P. Bakkers, Twinning superlattices in indium phosphide nanowires, Nature 456 (7220) (2008) 369–372.
[7] P. Caroff, K.A. Dick, J. Johansson, M.E. Messing, K. Deppert, L. Samuelson, Controlled polytypic and twin-plane superlattices in III–V nanowires, Nature Nanotechnology 4 (1) (2009) 50–55.
[8] B. Jacobs, V. Ayres, M. Crimp, K. McElroy, Internal structure of multiphase zinc-blende wurtzite gallium nitride nanowires, Nanotechnology 19 (40) (2008) 405706.
[9] K.A. Dick, C. Thelander, L. Samuelson, P. Caroff, Crystal phase engineering in single InAs nanowires, Nano Lett. 10 (9) (2010) 3494–3499.
[10] D. Spirkoska, J. Arbiol, A. Gustafsson, S. Conesa-Boj, F. Glas, I. Zardo, M. Heigoldt, M. Gass, A.L. Bleloch, S. Estrade, et al., Structural and optical properties of high quality zinc-blende/wurtzite GaAs nanowire heterostructures, Phys. Rev. B—Condensed Matter Mater. Phys. 80 (24) (2009) 245325.
[11] M. Tan, T. Gao, Q. Xiao, Y. Gao, Y. Liu, Q. Xie, Q. Chen, Z. Tian, Y. Liang, B. Wang, Simulation study on the diversity and characteristics of twin structures in GaN, Superlattices Microstruct. 159 (2021) 107037.
[12] C.-Y. Yeh, Z. Lu, S. Froyen, A. Zunger, Predictions and systematizations of the zinc-blende–wurtzite structural energies in binary octet compounds, Phys. Rev. B 45 (20) (1992) 12130.
[13] T. Akiyama, K. Sano, K. Nakamura, T. Ito, An empirical potential approach to wurtzite–zinc-blende polytypism in group III–V semiconductor nanowires, Japan. J. Appl. Phys. 45 (3L) (2006) L275.
[14] L. Zhang, M. Yang, S. Zhang, H. Niu, Unveiling the crystallization mechanism of cadmium selenide via molecular dynamics simulation with machine-learning-based deep potential, J. Mater. Sci. Technol. 185 (2024) 23–31.
[15] Y. Gao, B. Wang, J. Huang, T. Gao, W. Yang, Q. Xie, Q. Chen, Growth pattern of homogeneous and heterogeneous nucleation in high-entropy FeNiCrCoCu alloys, Cryst. Growth & Des. 22 (4) (2022) 2417–2425.
[16] A.H. Zahiri, M. Lotfpour, J. Ombogo, E. Vitral, L. Cao, The anisotropy of deformation twinning in bcc materials: Mechanical loading, temperature effect, and twin–twin interaction, Acta Mater. 266 (2024) 119681.
[17] A.H. Zahiri, J. Ombogo, M. Lotfpour, L. Cao, Twinning in Hexagonal close-packed materials: The role of phase transformation, Metals 13 (3) (2023) 525.
[18] A.H. Zahiri, E. Vitral, J. Ombogo, M. Lotfpour, L. Cao, The role of mechanical loading in bcc-hcp phase transition: tension-compression asymmetry and twin formation, Acta Mater. 241 (2022) 118377.
[19] A.H. Zahiri, J. Ombogo, L. Cao, Formation of {112¯ 2} contraction twins in titanium through reversible martensitic phase transformation, Scr. Mater. 195 (2021) 113694.
[20] J. Ombogo, A.H. Zahiri, T. Ma, L. Cao, Nucleation of {10 1¯ 2} twins in magnesium through reversible martensitic phase transformation, Metals 10 (8) (2020) 1030.
[21] S. Plimpton, P. Crozier, A. Thompson, LAMMPS-large-scale atomic/molecular massively parallel simulator, Sandia Natl. Lab. 18 (2007) 43.
[22] A. Béré, A. Serra, On the atomic structures, mobility and interactions of extended defects in GaN: dislocations, tilt and twin boundaries, Phil. Mag. 86 (15) (2006) 2159–2192.
[23] W.G. Hoover, Canonical dynamics: Equilibrium phase-space distributions, Phys. Rev. A 31 (3) (1985) 1695.
[24] S. Nosé, A unified formulation of the constant temperature molecular dynamics methods, J. Chem. Phys. 81 (1) (1984) 511–519.
[25] M. Kaviany, Heat Transfer Physics, Cambridge University Press, 2008.
[26] P.K. Schelling, S.R. Phillpot, P. Keblinski, Comparison of atomic-level simulation methods for computing thermal conductivity, Phys. Rev. B 65 (14) (2002) 144306.
[27] D.P. Sellan, E.S. Landry, J. Turney, A.J. McGaughey, C.H. Amon, Size effects in molecular dynamics thermal conductivity predictions, Phys. Rev. B—Condensed Matter Mater. Phys. 81 (21) (2010) 214305.
[28] Y. Wang, B. Qiu, X. Ruan, Edge effect on thermal transport in graphene nanoribbons: A phonon localization mechanism beyond edge roughness scattering, Appl. Phys. Lett. 101 (1) (2012).
[29] P. Chakraborty, L. Cao, Y. Wang, Ultralow lattice thermal conductivity of the random multilayer structure with lattice imperfections, Sci. Rep. 7 (1) (2017) 8134.
[30] H. Cui, T. Maranets, T. Ma, Y. Wang, Spectral analysis of coherent and incoherent phonon transport in silicon nanomeshes, Phys. Rev. B 110 (2024) 075301, http://dx.doi.org/10.1103/PhysRevB.110.075301, URL https://link.aps.org/doi/10.1103/PhysRevB.110.075301.
[31] H. Cui, T. Ma, Y. Wang, Elucidating optimal nanohole structures for suppressing phonon transport in nanomeshes, 2d Mater. 11 (3) (2024) 035026.
[32] C.-Y. Yeh, Z. Lu, S. Froyen, A. Zunger, Zinc-blende–wurtzite polytypism in semiconductors, Phys. Rev. B 46 (16) (1992) 10086.
[33] A.B. Aebersold, L. Fanni, A. Hessler-Wyser, S. Nicolay, C. Ballif, C. Hébert, D.T. Alexander, Zinc blende–wurtzite polytypism in nanocrystalline ZnO films, Acta Mater. 130 (2017) 240–248.
[34] Y. Ding, Z.L. Wang, T. Sun, J. Qiu, Zinc-blende ZnO and its role in nucleating wurtzite tetrapods and twinned nanowires, Appl. Phys. Lett. 90 (15) (2007).
[35] A. Fiore, R. Mastria, M.G. Lupo, G. Lanzani, C. Giannini, E. Carlino, G. Morello, M. De Giorgi, Y. Li, R. Cingolani, et al., Tetrapod-shaped colloidal nanocrystals of II- VI semiconductors prepared by seeded growth, J. Am. Chem. Soc. 131 (6) (2009) 2274–2282.
[36] B. O'malley, I. Snook, Crystal nucleation in the hard sphere system, Phys. Rev. Lett. 90 (8) (2003) 085702.
[37] J.-M. Leyssale, J. Delhommelle, C. Millot, Reorganization and growth of metastable α-N2 critical nuclei into stable β-N2 crystals, J. Am. Chem. Soc. 126 (39) (2004) 12286–12287.
[38] G. Razul, J. Hendry, P. Kusalik, Mechanisms of heterogeneous crystal growth in atomic systems: Insights from computer simulations, J. Chem. Phys. 123 (20) (2005).

[39] Z.-a. Tian, L.-l. Zhou, Y.-f. Mo, Y.-c. Liang, R.-s. Liu, Cooling rate dependence of polymorph selection during rapid solidification of liquid metal zinc, Trans. Nonferr. Met. Soc. China 25 (12) (2015) 4072–4079.
[40] A. Stukowski, Visualization and analysis of atomistic simulation data with OVITO–the Open Visualization Tool, Modelling Simul. Mater. Sci. Eng. 18 (1) (2009) 015012.
[41] H. Zheng, J. Wang, J.Y. Huang, J. Wang, Z. Zhang, S.X. Mao, Dynamic process of phase transition from wurtzite to zinc blende structure in InAs nanowires, Nano Lett. 13 (12) (2013) 6023–6027.
[42] N. Li, S.K. Yadav, J. Wang, X.-Y. Liu, A. Misra, Growth and stress-induced transformation of zinc blende AlN layers in Al-AlN-TiN multilayers, Sci. Rep. 5 (1) (2015) 18554.
[43] J. Lähnemann, U. Jahn, O. Brandt, T. Flissikowski, P. Dogan, H.T. Grahn, Luminescence associated with stacking faults in GaN, J. Phys. D: Appl. Phys. 47 (42) (2014) 423001.
[44] S. Ruvimov, O. Manasreh, Defect engineering in III-nitrides epitaxial systems, in: III-Nitride Semiconductors: Electrical, Structural and Defects Properties, Elsevier Amsterdam, 2000, pp. 51–75.
[45] C. Stampfl, C.G. Van de Walle, Energetics and electronic structure of stacking faults in AlN, GaN, and InN, Phys. Rev. B 57 (24) (1998) R15052.
[46] B. Li, Q. Sun, X. Zhang, Lattice correspondence analysis on the formation mechanism for partial stacking faults in hexagonal close-packed metals, Comput. Mater. Sci. 198 (2021) 110684.
[47] L.-Y. Tian, R. Lizárraga, H. Larsson, E. Holmström, L. Vitos, A first principles study of the stacking fault energies for fcc Co-based binary alloys, Acta Mater. 136 (2017) 215–223.
[48] C. Dai, Q. Wang, P. Saidi, B. Langelier, C. Judge, M. Daymond, M. Mattucci, Atomistic structure and thermal stability of dislocation loops, stacking fault tetrahedra, and voids in face-centered cubic Fe, J. Nucl. Mater. 563 (2022) 153636.
[49] L. Lindsay, D.A. Broido, T.L. Reinecke, Thermal conductivity and large isotope effect in GaN from first principles, Phys. Rev. Lett. 109 (2012) 095901, http://dx.doi.org/10.1103/PhysRevLett.109.095901, URL https://link.aps.org/doi/10.1103/PhysRevLett.109.095901.
[50] R. Wu, R. Hu, X. Luo, First-principle-based full-dispersion Monte Carlo simulation of the anisotropic phonon transport in the wurtzite GaN thin film, J. Appl. Phys. 119 (14) (2016).
[51] Q. Zheng, C. Li, A. Rai, J.H. Leach, D.A. Broido, D.G. Cahill, Thermal conductivity of GaN, ^{71}GaN, and SiC from 150 K to 850 K, Phys. Rev. Mater. 3 (2019) 014601, http://dx.doi.org/10.1103/PhysRevMaterials.3.014601, URL https://link.aps.org/doi/10.1103/PhysRevMaterials.3.014601.
[52] D.Q. Tran, T. Paskova, V. Darakchieva, P.P. Paskov, On the thermal conductivity anisotropy in wurtzite GaN, AIP Adv. 13 (9) (2023).
[53] Z. Sun, Z. Qi, K. Liang, X. Sun, Z. Zhang, L. Li, Q. Wang, G. Zhang, G. Wu, W. Shen, A neuroevolution potential for predicting the thermal conductivity of α, β, and ε-Ga2O3, Appl. Phys. Lett. 123 (19) (2023).
[54] Z. Qi, X. Sun, Z. Sun, Q. Wang, D. Zhang, K. Liang, R. Li, D. Zou, L. Li, G. Wu, et al., Interfacial optimization for AlN/diamond heterostructures via machine learning potential molecular dynamics investigation of the mechanical properties, ACS Appl. Mater. & Interfaces 16 (21) (2024) 27998–28007.
[55] Z. Sun, D. Zhang, Z. Qi, Q. Wang, X. Sun, K. Liang, F. Dong, Y. Zhao, D. Zou, L. Li, et al., Insight into interfacial heat transfer of β-Ga2O3/diamond heterostructures via the machine learning potential, ACS Appl. Mater. & Interfaces 16 (24) (2024) 31666–31676.
[56] Z. Sun, Y. Song, Z. Qi, X. Sun, M. Liao, R. Li, Q. Wang, L. Li, G. Wu, W. Shen, et al., Heat transport exploration through the GaN/diamond interfaces using machine learning potential, Int. J. Heat Mass Transfer 241 (2025) 126724.
[57] H. Cui, I.R. Panneerselvam, P. Chakraborty, Q. Nian, Y. Liao, Y. Wang, Significantly enhanced interfacial thermal transport between single-layer graphene and water through basal-plane oxidation, Carbon 234 (2025) 119910.
[58] J. Callaway, Model for lattice thermal conductivity at low temperatures, Phys. Rev. 113 (4) (1959) 1046.
[59] T. Ma, P. Chakraborty, X. Guo, L. Cao, Y. Wang, First-principles modeling of thermal transport in materials: Achievements, opportunities, and challenges, Int. J. Thermophys. 41 (2020) 1–37.
[60] P.E. Hopkins, Multiple phonon processes contributing to inelastic scattering during thermal boundary conductance at solid interfaces, J. Appl. Phys. 106 (1) (2009).
[61] K. Sääskilahti, J. Oksanen, J. Tulkki, S. Volz, Role of anharmonic phonon scattering in the spectrally decomposed thermal conductance at planar interfaces, Phys. Rev. B 90 (13) (2014) 134312.
[62] P. Chakraborty, I.A. Chiu, T. Ma, Y. Wang, Complex temperature dependence of coherent and incoherent lattice thermal transport in superlattices, Nanotechnology 32 (6) (2020) 065401.
[63] I.R. Panneerselvam, H. Cui, T. Maranets, Y. Wang, Disorder-dominated and scattering-dominated thermal transport in clathrate hydrates, Comput. Mater. Sci. 244 (2024) 113189.
[64] H. Cui, T. Maranets, T. Ma, Y. Wang, Spectral heat flux redistribution upon interfacial transmission, J. Phys.: Condens. Matter. 37 (11) (2025) 115002.
[65] E. Landry, M. Hussein, A. McGaughey, Complex superlattice unit cell designs for reduced thermal conductivity, Phys. Rev. B—Condensed Matter Mater. Phys. 77 (18) (2008) 184302.
[66] Y. Wang, H. Huang, X. Ruan, Decomposition of coherent and incoherent phonon conduction in superlattices and random multilayers, Phys. Rev. B 90 (16) (2014) 165406.
[67] R. Hu, S. Iwamoto, L. Feng, S. Ju, S. Hu, M. Ohnishi, N. Nagai, K. Hirakawa, J. Shiomi, Machine-learning-optimized aperiodic superlattice minimizes coherent phonon heat conduction, Phys. Rev. X 10 (2) (2020) 021050.
[68] P. Chakraborty, Y. Liu, T. Ma, X. Guo, L. Cao, R. Hu, Y. Wang, Quenching thermal transport in aperiodic superlattices: A molecular dynamics and machine learning study, ACS Appl. Mater. & Interfaces 12 (7) (2020) 8795–8804.
[69] J. Ravichandran, A.K. Yadav, R. Cheaito, P.B. Rossen, A. Soukiassian, S. Suresha, J.C. Duda, B.M. Foley, C.-H. Lee, Y. Zhu, et al., Crossover from incoherent to coherent phonon scattering in epitaxial oxide superlattices, Nat. Mater. 13 (2) (2014) 168–172.
[70] Y. Wang, C. Gu, X. Ruan, Optimization of the random multilayer structure to break the random-alloy limit of thermal conductivity, Appl. Phys. Lett. 106 (7) (2015).
[71] Y. Wang, X. Ruan, A.K. Roy, Two-temperature nonequilibrium molecular dynamics simulation of thermal transport across metal-nonmetal interfaces, Phys. Rev. B—Condensed Matter Mater. Phys. 85 (20) (2012) 205311.
[72] K.R. Hahn, M. Puligheddu, L. Colombo, Thermal boundary resistance at Si/Ge interfaces determined by approach-to-equilibrium molecular dynamics simulations, Phys. Rev. B 91 (19) (2015) 195313.
[73] E.T. Swartz, R.O. Pohl, Thermal boundary resistance, Rev. Modern Phys. 61 (1989) 605–668, http://dx.doi.org/10.1103/RevModPhys.61.605, URL https://link.aps.org/doi/10.1103/RevModPhys.61.605.
[74] R. Prasher, Acoustic mismatch model for thermal contact resistance of van der Waals contacts, Appl. Phys. Lett. 94 (4) (2009).
[75] M. Nasiri, Y. Wang, Evolution of phonon spectral energy density in superlattice structures, Crystals 15 (5) (2025) http://dx.doi.org/10.3390/cryst15050446, URL https://www.mdpi.com/2073-4352/15/5/446.